The International Journal of Advanced Manufacturing Technology
https://doi.org/10.1007/s00170-024-14096-4

ORIGINAL ARTICLE

Nugget and corona bond size measurement through active thermography and transfer learning model

Luca Santoro[1] · **Valentino Razza**[2] · **Manuela De Maddis**[2]

Received: 18 March 2024 / Accepted: 1 July 2024
© The Author(s) 2024

Abstract
Resistance spot welding (RSW) is considered a preferred technique for joining metal parts in various industries, mainly for its efficiency and cost-effectiveness. The mechanical properties of spot welds are pivotal in ensuring structural integrity and overall assembly performance. In this work, the quality attributes of resistance spot welding, such as both nugget and corona bond sizes, are assessed by analyzing the thermal behavior of the joint using a physical information neural network (PINN). Starting from the thermal signal phase gradient and amplitude gradient maps, a convolutional neural network (CNN) estimates the size of nuggets and corona bonds. The CNN architecture is based on the Inception V3 architecture, a state-of-the-art neural network that excels in image recognition tasks. This study suggests adopting a new methodology for automatic RSW quality control based on thermal signal analysis.

Keywords Resistance spot weld · Quality · Convolutional neural network · Thermography · Welding

1 Introduction

Resistance spot welding (RSW) is a highly favored method for assembling metal components in various industries, mainly due to its efficiency and cost-effectiveness. The mechanical properties of the welding spots must be checked to guarantee the integrity of the assembly. Traditionally, weld quality assessment relies on destructive testing methods, such as peel and chisel tests, alongside evaluations of weld nugget characteristics, like shape and size. These methodologies have been the cornerstone for accurately determining welding quality.

Over the years, many researchers have studied the relationship between the welding process parameters and joint quality. For instance, [1] delve into the impact of electrode pressure on nugget size and its consequent influence on the tensile shear strength of the joint. Complementing this, [2] examine the effects of microstructural changes and nugget dimensions on the mechanical properties of DP600 steel when subjected to RSW. Furthermore, the phenomenon known as *expulsion*, which markedly affects the joint's mechanical properties, has been thoroughly investigated in studies such as [3] and [4, 5]. Meanwhile, [6] provide a comprehensive review of various RSW quality assessment methods, pinpointing the nugget diameter as a significant quality indicator. However, it is noted that this alone cannot serve as an ultimate criterion for mechanical quality assessment. The ISO standards and also the American Welding Society's standards, AWS D8.1M:2013 [7] and AWS D8.9M:2022 [8], suggest a range of inspection methods to determine weld quality, which can be customized for specific applications through agreements between customers and suppliers. The industry-standard destructive inspections ensure a minimum nugget diameter for adequate load resistance and to detect expulsion-related defects, which could significantly weaken the weld [9].

✉ Luca Santoro
luca.santoro@polito.it

Valentino Razza
valentino.razza@polito.it

Manuela De Maddis
manuela.demaddis@polito.it

[1] Department of Mechanical and Aerospace Engineering, Politecnico di Torino, Corso Duca degli Abruzzi 24, Torino 10129, Italy

[2] Department of Management and Production Engineering, Politecnico di Torino, Corso Duca degli Abruzzi 24, Torino 10129, Italy

Published online: 10 July 2024

The necessity to monitor weld quality and process stability has traditionally led to the adoption of destructive testing, which, while effective, results in the loss of a portion of the production, thereby increasing time and cost for the manufacturing process. This sample-based approach also means that many defective welds may remain undetected, compelling manufacturers to perform more welds than technically necessary [10–12].

NDT methods have become a focal point of research for identifying a good weld without resorting to destruction, incorporating techniques such as radiographic or ultrasonic inspections. However, these methods face challenges, including being time-consuming, cost-ineffective, and susceptible to human and environmental factors [11, 13–16].

Furthermore, in [17], authors point out the problem of the corona bond identification in ultrasonic testing; the corona bond, being welded but not melted as the nugget, has to be assessed during ultrasonic testing.

In light of this, thermographic testing and monitoring, which offers a noncontact approach to capture the thermal behavior from a sample surface, have been subject to extensive study. This is detailed in a vast literature [18–43].

Active or stimulated thermography is a highly promising approach in thermographic testing. It involves externally heating the examined component to analyze its thermal properties or identify any flaws. This method has demonstrated significant efficacy in examining welding microstructures and detecting defects, particularly in composite and laminate materials [32, 35, 44]. It differentiates between photo-thermal stimulation, which applies heat on the surface, and volumetric stimulation, generating heat within the material. Notably, ultrasound and electromagnetic induction have shown promise as methods for volumetric stimulation, achieving success in detecting flaws in metal structures and welds [23, 45–48]. Compared to other NDTs, thermography has several advantages. The required equipment is relatively cheap, the examined component does not need preparation, it is a contactless technique, and it can be fully automatized, i.e., human operators are not required during the data acquisition, preserving safety.

Particularly for detecting surface cracks or assessing weld joint quality, active thermography's role in NDT has been underscored through various stimulation techniques, including laser and lamp sources [22, 49–52]. Beyond mere defect detection, [53, 54] offer insights into the characteristics of the welded area and microstructural properties. In [55], the authors extend the study to use the thermographic nondestructive evaluation to assess the mechanical properties of the resistance projection weld joints. The authors use pulsed phase thermography to evaluate the welded area through the thermal phase delay. The welded area is evaluated by image segmentation based on value thresholding, while flash lamps provide thermal excitation.

Similarly in [55], active thermography has been used for non-destructive testing of probeless friction stir spot weld.

- This research arises from the industrial necessity of a quick and automated method for the non-destructive evaluation of welded joints. Resistance spot weld process is usually applied in high-volume assemblies requiring a high number of welding spots. Active thermography, being a noncontact method, well suits this aim. However, as with other methods presented, we still need the human interpretation of the results. This work proposes a methodology for automating the measurement of the nugget size through active thermography.

A similar approach used in the *Lock-In thermography* [56–58] is used, where a repeated step pulse modulated at a specific modulation frequency, i.e., the *lock-in frequency*, is applied to the specimen. On the other hand, the algorithm presented here allows for more advanced signal processing techniques, resulting in more consistent and accurate results. This research extends the findings of [59] by employing a convolutional neural network trained on the phase gradient and amplitude gradient of the thermal signal to estimate the nuggets and corona bond sizes. The study showcases the potential for automating the measurement of nugget size and corona bond. It is worth noting that convolutional neural network training requires a large amount of data and several epochs. From the literature, several papers exploit curriculum learning to transfer knowledge from a pre-trained network to other contexts. In image recognition, Imagenet is a well-known network trained for general purposes. Some applications are [60], where the main problem is to classify or segment an image to detect some properties, e.g., defects or anomalies. In this work, instead, we exploit the transfer learning technique to use the Inception V3 architecture with pre-trained weight on the Imagenet dataset, so a transfer learning model to estimate the nugget and corona bond size, i.e., making it a regression problem. In this way, this algorithm can be exploited for fully automated inspection systems to generate reports on a large number of inspected joints.

The paper develops as follows: Sect. 2 discusses the analytical background of thermal phase analysis. Section 3 outlines the RSW process, the active thermography setup, and the proposed methodology for data analysis. Results showing the effectiveness of the proposed NDT method to measure the nugget and corona bond sizes are presented in Sect. 4. Conclusion and future remarks end the paper.

2 Analytical background

2.1 Thermal diffusivity

The underlying concept of this study is that both the thickness and thermal diffusivity impact the thermal phase measured through the plane.

We begin this section by presenting the mathematical model that explains the thermal characteristics of a single slab under an external thermal stimulus. The theoretical framework presented here is derived from the findings in [61]. A scenario is considered where a laser beam interacts with a slab of thickness ℓ. For simplicity, the slab is assumed to be opaque with a surface extending infinitely. The laser beam, with power P_0, is described by a Gaussian distribution with a radius of a at $1/e^2$. Consequently, the laser power transmitted to the sample is

$$P(r) = \eta \frac{P_0}{\pi a^2} e^{-2r^2/a^2}, \tag{1}$$

where η is the power fraction absorbed, and $r \geq 0$ is the distance from the center of the laser spot, as shown in Fig. 1.

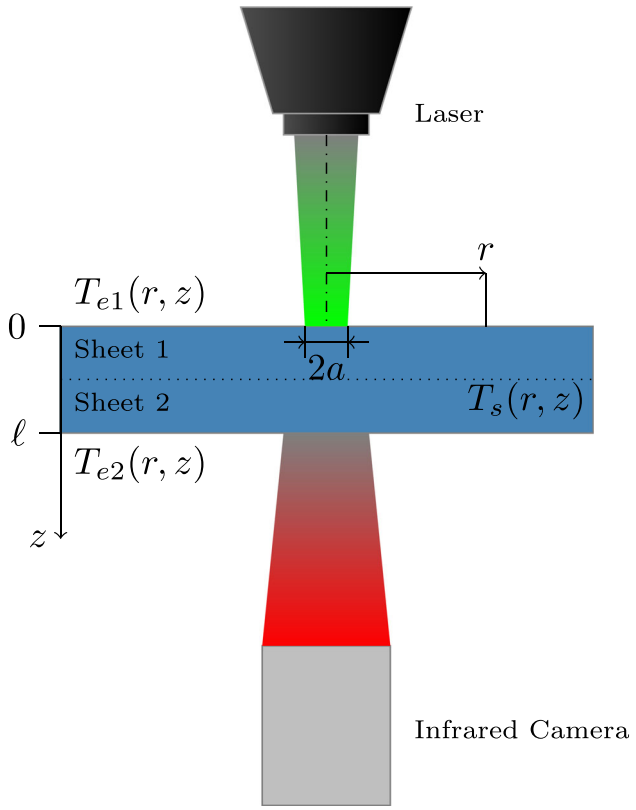

Fig. 1 Cross-section of the experimental setup and the reference system. The laser excites one side of the specimen, while the infrared camera acquires the thermal behavior on the opposite one

The slab is assumed to be in contact with air, and the laser beam undergoes modulation at a frequency f_ℓ (i.e., $\omega_\ell = 2\pi f_\ell$). The analysis focuses solely on the oscillatory part of the temperature $T(r, z)$, where z is the perpendicular direction to the specimen surface (see Fig. 1). The heated and rear surfaces are distinguished by subscripts $e1$ and $e2$, respectively, while the sample is denoted by the subscript s (refer to Fig. 1). Given the cylindrical symmetry of the considered model, the oscillatory temperature components of each medium are expressed through the Hankel transforms:

$$T_{e1}(r,z) = \int_0^\infty \delta J_0(\delta r) K_1 e^{\beta_e z} d\delta, \text{ if } z \leq 0, \tag{2a}$$

$$T_s(r,z) = \int_0^\infty \delta J_0(\delta r) \left[K_2 e^{-\beta_s z} + K_3 e^{\beta_s z}\right] d\delta, \text{ if } 0 \leq z \leq \ell, \tag{2b}$$

$$T_{e2}(r,z) = \int_0^\infty \delta J_0(\delta r) K_4 e^{\beta_e(-z+\ell)} d\delta, \text{ if } z \geq \ell, \tag{2c}$$

where J_0 is the Bessel function of the 0-th order, δ is the Hankel variable, $\beta_x^2 = \delta^2 + i\omega/D_x$, $x = \{e, s\}$, and $i = \sqrt{-1}$. D_e and D_s are the air and sample diffusion coefficients, respectively, and $K_i, i = 1, \ldots, 4$ are constant coefficients determined from the boundary conditions that guarantee the temperature continuity along the slab boundaries:

$$T_{e1}(r,0) = T_s(r,0) \tag{3a}$$

$$T_{e2}(r,\ell) = T_s(r,\ell). \tag{3b}$$

and the heat transfer equilibrium along the surfaces (by convection and radiation), i.e.,

$$\begin{aligned} -K_s \left.\frac{\partial T_s}{\partial z}\right|_{z=0} &= -K_e \left.\frac{\partial T_{e1}}{\partial z}\right|_{z=0} + h T_s\Big|_{z=0} \\ &\quad - \eta \frac{P_0}{2\pi} \int_0^\infty \delta J_0(\delta r) e^{(\delta a)^2/8} d\delta, \end{aligned} \tag{4a}$$

$$-K_s \left.\frac{\partial T_s}{\partial z}\right|_{z=\ell} = -K_e \left.\frac{\partial T_{e2}}{\partial z}\right|_{z=\ell} + h T_s\Big|_{z=\ell}, \tag{4b}$$

where K_e and K_s are the air and sample thermal conductivity, respectively. h is the heat transfer coefficient, which considers the combined effect of convection and radiation on the outer surfaces. By combining (2)–(4), the overall oscillating components slab temperature equation is

$$\begin{aligned} T_s(r,z) = \frac{\eta P_0}{4\pi} \int_0^\infty \delta J_0(\delta r) e^{-(\delta a)^2/8} \\ \times \frac{A e^{-\beta_s(z-\ell)} + B e^{\beta_s(z-\ell)}}{A^2 e^{\beta_s \ell} - B^2 e^{-\beta_s \ell}} d\delta, \end{aligned} \tag{5}$$

where $A = K_s\beta_s + K_g\beta_g + h$ and $B = K_s\beta_s - K_g\beta_g - h$. An interested reader may refer to [61] for further details on the slab temperature model.

In our application, the sample is made of steel, characterized by thermal conductivity $K_s \gg K_e$ (for air, the standard value at ambient temperature $K_e \approx 0.025\,\mathrm{W\,m^{-1}\,K^{-1}}$). Moreover, for non-low frequency f, i.e., $f \geq 1$ Hz, $K_e\beta_e \ll K_s\beta_s$, and $h \ll K_s\beta_s$, and Eq. 5 can be rewritten as

$$T_s(r,z) \approx \frac{\eta P_0}{4\pi K_s}\int_0^\infty \delta J_0(\delta r)\frac{e^{-(\delta a)^2/8}}{\beta_s} \times \frac{e^{-\beta_s(z-\ell)}+e^{\beta_s(z-\ell)}}{e^{\beta_s\ell}-e^{-\beta_s\ell}}d\delta. \tag{6}$$

We are interested in evaluating the rear sample temperature acquired by an infrared camera. From Eq. 6, we get

$$T_s(r,\ell) \approx \frac{\eta P_0}{2\pi K_s}\int_0^\infty \frac{\delta J_0(\delta r)}{\beta_s}\frac{e^{-(\delta a)^2/8}}{e^{\beta_s\ell}-e^{-\beta_s\ell}}d\delta, \forall r \leq a. \tag{7}$$

By evaluating (7) at $\omega = \omega_\ell$ through numerical analysis, the laser power to the rear temperature phase delay inside the laser spot covered area is related to the laser pulsing frequency as

$$\phi = -\ell/\lambda, \tag{8}$$

where $\lambda = \sqrt{2D_s/\omega_\ell}$ is the thermal diffusion length (see [62] for further details).

Remark 1 It is worth noting that Eq. 8 does not account for nonlinearities due to small thermal diffusivity coefficient or low laser modulation frequency (see, e.g., [61]). From the authors' experience, the laser power must be set accordingly to have at least 10 °C temperature increase from ambient temperature to have reliable data.

2.2 Frequency analysis

On the contrary of the theoretical analysis given in Sect. 2.1, an RSW joint is not a uniform slab. Thickness changes due to the electrode marks and the internal microstructure change since the base material reached fusion. Thus, the phase delay (8) is not uniform along the sample rear surface, and the differences account for the RWS structure.

The temperature profile on the sample rear side is measured through a thermal camera. Along an observation period of length $N\tau_s$, we get the 3D matrix whose entries are $T_k^{(x,y)}$, where $k = 0,\ldots,N-1$ is the discrete sample time $t = k\tau_s$, τ_s is the camera sampling time, and N is the number of frames acquired. $x = 0,\ldots W-1$ and $y = 0,\ldots H-1$ are the frame column and row index, respectively, given the frame size $H \times W$. By selecting a single pixel index (x, y), we get the 1-dimensional vector, defined by the thermal behavior of the selected point $T_k^{(x,y)}$. For the sake of simplicity in the notation, we omit the pixel index (x, y) in the latter unless it is necessary for the algorithm, i.e., $T_k = T_k^{(x,y)}$. We must extract the oscillatory temperature components to compare the acquired thermal behavior T_k to the theoretical analysis from Sect. 2.1. It is worth noting that the previously used Hankel transform is the multidimensional Fourier transform, used to analyze in the frequency domain a signal propagating within the space.

Given the original formulation, the Fourier Transform requires processing a continuous-time signal. However, due to the intrinsic sampling from the thermal camera at a given frame rate, only the sampled signal sequence T_k is known for each pixel frame. The *Discrete Fourier Signal* (DFT) (see, e.g., [63])

$$\tilde{T}_n = \sum_{k=0}^{N-1} T_k\, e^{-\frac{i2\pi nk}{N}} \in \mathbb{C},\ \forall n = 0,\ldots,N-1. \tag{9}$$

converts a uniformly sampled sequence T_k into a sequence of N complex numbers denoted by $\tilde{T}_n$, whose amplitude and phase are related to sinusoidal signals at frequency $f = n/(N\tau_s)$. The original signal T_k can be retrieved through the linear combination of all the N sinusoids defined by $\tilde{T}_n$.

Since the laser source is modulated at the frequency f_ℓ, we limit the overall frequency analysis to the corresponding value $n_\ell = \lceil N\ \tau_s\ f_\ell \rceil$, i.e., to the same input frequency component.

By applying (9) to the temperature behavior of each pixel, we get a complex-valued matrix $\tilde{\mathbf{T}} = (\tilde{T}^{(x,y)}) \in \mathbb{C}^{H\times W}$. To manage real numbers only in the latter, we decompose the matrix $\tilde{\mathbf{T}}$ in the amplitude $|\tilde{\mathbf{T}}| = (|\tilde{T}^{(x,y)}|) \in \mathbb{R}^{H\times W}$ and phase $\angle\tilde{\mathbf{T}} = (\angle\tilde{T}^{(x,y)}) \in \mathbb{R}^{H\times W}$ matrices, where

$$|\tilde{T}| = \sqrt{\mathbf{I}\left\{\tilde{T}\right\}^2 + \mathbf{R}\left\{\tilde{T}\right\}^2}, \tag{10}$$

$$\angle\tilde{T} = \mathrm{atan2}\left(\mathbf{I}\left\{\tilde{T}\right\}, \mathbf{R}\left\{\tilde{T}\right\}\right). \tag{11}$$

$\mathrm{atan2}(b,a) \in [-\pi,\pi]$ is the angle measure between the positive real-axis and the ray joining the origin of the complex plane to the point $a+ib$, $\mathbf{R}(\cdot)$ and $\mathbf{I}(\cdot)$ are the argument real and imaginary part, respectively. $\angle\tilde{T}^{(x,y)}$ represents the laser to rear temperature delay at (x, y) position. All the values in $\angle\tilde{\mathbf{T}}$ are affected by the same uncertain term ϕ_0 due to the experimental delay between laser and camera synchronization. Thus, we get

$$\phi = \angle\tilde{T}_{n_\ell}^{(x,y)} - \phi_0, \tag{12}$$

From $\angle\tilde{T}_{n_\ell}$, it is possible to evaluate the *through-plane* thermal diffusivity. In fact, from Eqs. 8 and 12, for each pixel, the following relation holds:

$$\frac{\angle\tilde{T}^{(x,y)} - \phi_0}{\ell} = \sqrt{\frac{\pi f_\ell}{D_s}}. \tag{13}$$

The uncertainty given by ϕ_0 is solved by comparing, i.e., through difference, the entries of $\angle\tilde{\mathbf{T}}$.

3 Materials and methods

3.1 RSW process

The spot welds have been obtained using an industrial medium frequency direct current (MFDC) RSW machine.

The experimental tests are conducted on coupons made on DP590 galvanized steel sheets, commonly used to produce car body parts, 1 mm thick, using Cu-Cr-Zr electrodes with a truncated cone shape with a nominal contact diameter of 6 mm. During the welding procedure, the electrodes have been cooled through a water flow of about 4 L min^{-1}.

The welding procedure and the face diameter of the electrodes have been chosen based on the recommendations from [8]. The squeeze and hold times have been kept at 100 ms and 300 ms, respectively.

The optimal process parameter has been chosen to obtain the best mechanical characteristics: no-splash, a nugget size about four times the square root of the thickness of the sheet according to [8], and minimum tensile shear strength (TSS) required by the standard higher than 5 kN with pull-out mode fracture.

Following the standard recommendations to construct the weldability lobe at constant weld time (200 ms), 78 spot welds have been performed, resulting in a wide range of nugget diameter values including conditions outside the accepted limits and the presence of spatter. The test campaign is summarized in Table 1.

The quality of a weld is usually expressed by some features, either from a direct visual inspection or measured through destructive tests. Commonly used weld attributes are nugget/ZTA, penetration, indentation/cracks (surface and internal), porosity/voids, sheet separation, and surface appearance. Among these attributes, weld size, evaluated as the nugget diameter, is the most frequently measured and meaningful in determining weld strength. However, in some contexts, nugget size alone, which determines the area of fusion and its load-bearing capability, is insufficient in describing a weld quality, as it does not necessarily imply the structural integrity of the weld. For example, a reduction in tensile and shear strength may be due to an increase in current, which leads to larger heat input and, thus, a reduction in the time required to reach melting temperature. The consequence is a larger nugget size, leading to sensitive variation in nugget diameter, reduced thickness, deeper electrode marks, and more significant deformations. Thus, other weld features, e.g., microstructural composition [1, 2] and hardness or presence of expulsion [4], may complement the nugget size and provide helpful information on the degree of adhesion.

3.2 Inspection

Weld performance is evaluated in terms of tensile–shear strength (peak load) and failure mode, e.g., interfacial fracture (in Fig. 4b) and pull-out (in Fig. 4a) [64].

The peak load in the tensile-shear test has been evaluated using the maximum load the weld can withstand. The shear tension samples have been carried out through a standard testing machine with a 10 mm min^{-1} crosshead speed.

The shear tension tests are 30 mm × 100 mm, with an overlapping area of 30 mm, according to JIS X 3136 (Japanese Standard Association 2018)

Furthermore, since the best parameter that describes mechanical properties is the nugget (see, e.g., [6]), metallurgical analysis has been performed to measure the geometry of the nugget and detect internal porosities. The specimens have been prepared by being cut in the half of the spot weld, mounted, polished with 1 µm diamond past, and then etched with Nital 1%. Finally, a macrography analysis of the welds is carried out employing a Zeiss Axio Observer microscope. In the resulting cross-section of the weld, it is possible to make

Table 1 Experimental parameters of spot welding (specimen n°)

Force[kN]/Current[kA]	8	9	10	11	12	12.5	13	14
2.1			9–12					
2.5	4–7						38–41	
2.9		73–76		21–24				77–78
3.3		17–20			61–64	34–37		
3.7	13–16		65–68				27–33	
4.1					56–59			42–45
4.6	52–55	46–49		69–72				

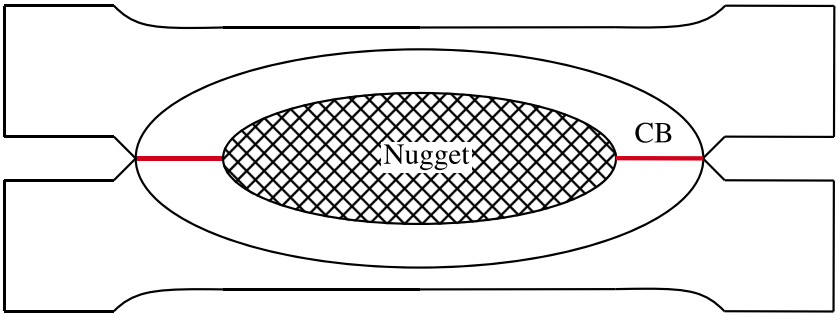

Fig. 2 Scheme of corona bond (CB) and nugget

several measurements defined as nugget and heat-affected zone (HAZ) dimensions, such as diameter and penetration and the depth of the electrode indentation [65].

The area subjected to welding, examined through non-destructive testing, is illustrated in Fig. 2. This region encompasses both the nugget and the surrounding corona bond area. Although the metal does not reach the melting temperature within the corona bond area, solid phase bonding is effectively achieved.

The size of the nugget mainly affects the mechanical strength of the joint. Figure 3 illustrates the linear relationship between the nugget diameter and the mechanical resistance of the joint, with the data points almost passing through the origin of the plot.

However, the correlation between the corona bond plus the nugget diameter and the ultimate tensile strength (UTS) of the joint shows more scattering and does not intersect the zero of the plot [66].

This observation highlights the need for higher safety factors when using standard non-destructive testing (NDT) methods to assess the mechanical properties of the joint, as these methods typically measure the corona bond plus the nugget diameter, representing the joined area. The nugget shape influences not only the mechanical resistance of the joint but also the failure mode. In Fig. 4, two different welds after the mechanical test are shown. It is possible to see how

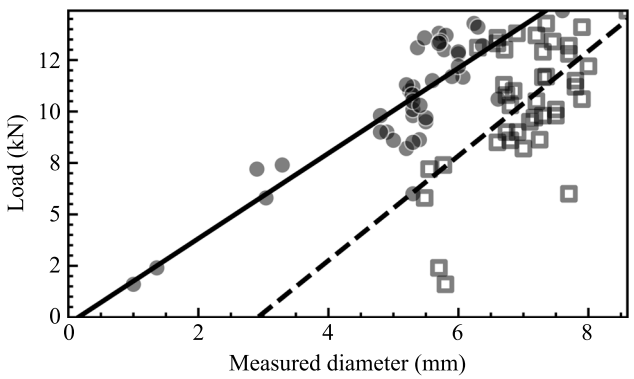

Fig. 3 Nugget (dots) and corona bond (squares) vs peak load and respective fitting lines for nugget (solid) and corona bond (dashed)

the nugget can be different from the heat-affected zone; the adhesion in the corona bond is broken during the mechanical test, while the nugget tends to stay integer and does not debond. This has a strong influence on the mechanical properties, and in the failure mode, being able to discern the nugget from the corona bond helps to understand the failure modes and mechanical behavior of the joint.

Experimental active thermography equipment comprises a thermal camera, a laser excitation source, and a PC control unit. The IR thermal camera is a cooled InSb FLIR A6750sc, having a sensitivity lower than 20 mK, equipped with a lens characterized by 50 mm focal length and a 3–5 μm spectral range. The laser source can generate a maximum power of 50 W concentrated in a circular spot 10 mm in diameter. The experimental configuration is set in transmission mode as shown in Fig. 1, and the setup parameters are presented in Table 2.

The experiments have been run at 26.0 °C room temperature, relative humidity 30%, and a distance between the laser source and the target of 530 mm. With this setup, the parameters regarding the Field of View are HFOV=200 mm, VFOV=160 mm, and an IFOV=0.32 mm.

3.3 Pre-processing

Given the video from the thermographic camera, we compute the matrices $|\tilde{\mathbf{T}}|$ and $\angle\tilde{\mathbf{T}}$, as shown in Sect. 2. Changes in the amplitude and phase matrix entries highlight differences from the uniform slub model considered in Sect. 2.1 and, thus, information about the internal joint structure.

To highlight such variations, we exploit the numerical gradients along the two dimensions, row and column, i.e.,

$$\nabla\mathbf{F} = \frac{\partial\mathbf{F}}{\partial x}\vec{i} + \frac{\partial\mathbf{F}}{\partial y}\vec{j}, \tag{14}$$

where $\mathbf{F}$ is one among the amplitude or the phase matrix, and $\vec{i}$ and $\vec{j}$ and the versors along x and y direction, respectively. It is worth noting that the Jocobian matrices $\frac{\partial\mathbf{F}}{\partial x} \in \mathbb{R}^{H\times W}$ and $\frac{\partial\mathbf{F}}{\partial y} \in \mathbb{R}^{H\times W}$ preserve the original matrix $\mathbf{F}$ sizes. The measure of the change rate is given from the element-wise

Fig. 4 Failure modes

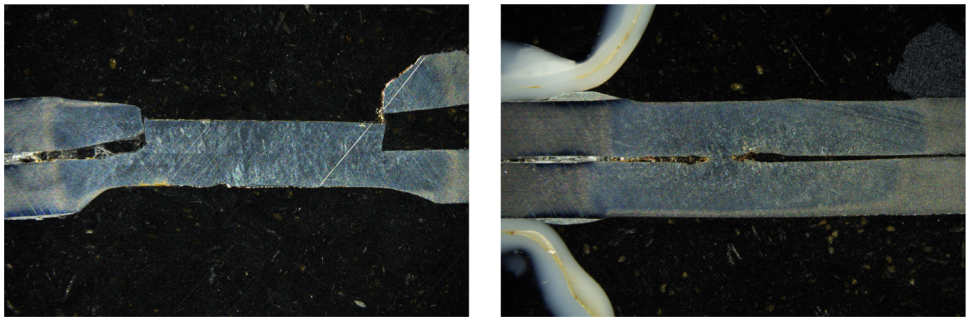

(a) no.48 - Pull Out (b) no.52 - Interfacial

gradient magnitude:

$$|\nabla \mathbf{F}| = \left(\sqrt{\left(\frac{\partial F^{(x,y)}}{\partial x} \right)^2 + \left(\frac{\partial F^{(x,y)}}{\partial y} \right)^2} \right), \tag{15}$$

To magnify the variations of $\nabla \mathbf{F}$ along the radial direction toward the spot center, we adjust the gradient as follows. Given a cartesian point (x_o, y_o),

$$\vec{c}(x_o, y_o) = (x_o - x_c)\vec{i} + (y_o - y_c)\vec{j} \tag{16}$$

is the oriented vector joining the spot center (x_c, y_c) to the considered point. From Eq. 14, we define the vector

$$\vec{g}(x_o, y_o) = \left. \frac{\partial F^{(x,y)}}{\partial x} \right|_{(x,y)=(x_o,y_o)} \vec{i} + \left. \frac{\partial F^{(x,y)}}{\partial y} \right|_{(x,y)=(x_o,y_o)} \vec{j} \tag{17}$$

as the gradient evaluated at (x_o, y_o). From the *dot* product property, we have

$$\cos\theta(x_o, y_o) = \frac{\vec{g}(x_o, y_o) \cdot \vec{c}(x_o, y_o)}{\|\vec{g}(x_o, y_o)\| \|\vec{c}(x_o, y_o)\|}, \tag{18}$$

where $\theta(x_o, y_o)$ is the angle between $\vec{c}(x_o, y_o)$ and $\vec{g}(x_o, y_o)$. For each point (x, y), the value $\cos\theta(x, y)$ is used to adjust $|\nabla \mathbf{F}|$ as

$$|\nabla \mathbf{F}|_{\text{adj}} = \left(|\nabla F^{(x,y)}| \cos\theta(x, y) \right). \tag{19}$$

Table 2 Active thermography set-up parameters

Modulation Frequency	0.5 Hz
N° of pulses	25
Laser power	50 W
Laser spot diamater	10 mm
Power density	0.64 W mm^{-1}
Acquisition frame rate	100 Hz
IR range	0-90 °C

This adjustment emphasizes gradient components that are more aligned with the vector towards the spot center (see Fig. 5), thereby enhancing features in the image that are radially oriented along the joint. Equation 19 is applied to both magnitude and phase matrices to compute the corresponding $|\nabla|\tilde{\mathbf{T}}||_{\text{adj}}$ and $|\nabla \angle \tilde{\mathbf{T}}|_{\text{adj}}$.

3.4 Neural network

The proposed algorithm exploits a neural network (NN) to parse together the matrices $|\nabla|\tilde{\mathbf{T}}||_{\text{adj}}$ and $|\nabla \angle \tilde{\mathbf{T}}|_{\text{adj}}$ and extract information about nuggets and corona bond widths. The information stored in those matrices has a precise meaning until the 2D dimensions are preserved. In fact, the nugget and corona bond shapes can be retrieved by comparing a pixel

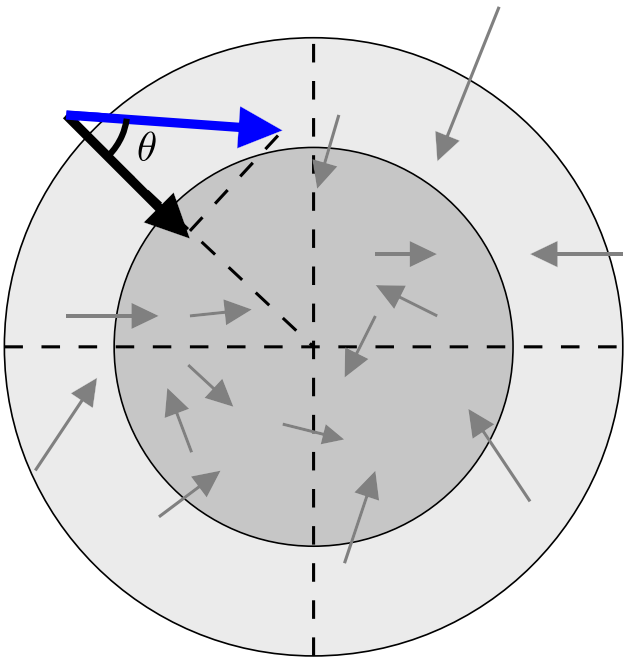

Fig. 5 Scheme of the adjusted gradient. Gray arrows represent the gradient vectors. Given the gradient vector at (x_o, y_o) (blue), the adjusted gradient vector toward the circle center is the projection along the desired direction (black)

with its neighbors in every direction. For this reason, we cannot unroll the matrices in a unique 1D vector, and the matrices parsing must include a spatial convolution. Training a convolutional neural network (CNN) requires a large amount of data that cannot be easily generated from experimental welding tests. It is worth noting that, within the signal processing community, the problem of training reliable CNNs to retrieve info from 2D convolution is a common procedure in image processing. Thus, we exploit a pre-trained general-purpose image parser neural network, whose output is parsed by a tailored dense neural network (DNN), which provides the nugget and corona bond sizes.

We exploit the InceptionV3 neural network (NN) feature extraction layers (see, e.g., [67]) to parse our $|\nabla|\tilde{\mathbf{T}}||_{\text{adj}}$ and $|\nabla\angle\tilde{\mathbf{T}}|_{\text{adj}}$ matrices. We have normalized the values within the [0, 1] range for each matrix, leading to a data structure resembling a gray-scale image. The InceptionV3 is tuned to parse RGB images, i.e., three color channel images, and the best performances are achieved for 299 × 299 pixel picture size. Thus, the gray-scale images achieved from $|\nabla|\tilde{\mathbf{T}}||_{\text{adj}}$ and $|\nabla\angle\tilde{\mathbf{T}}|_{\text{adj}}$ are colorized by copying the same normalized values to the three color layers. Then, the image is cropped to the desired size, centering the spot weld joint within the image.

The images are passed to the InceptionV3 NN with pre-trained weight from *imagenet*. Since pre-trained CNN is used in this phase as a feature extractor, the parameters of the Inception V3 layers are set as not trainable. In Fig. 6, an overview on the network architecture is presented.

Our model's foundation is the InceptionV3 architecture, a state-of-the-art neural network design that better performs in image recognition tasks. InceptionV3 is distinguished by its unique structure, which features multiple "Inception modules." Each module comprises several parallel towers of convolutional layers, with each tower having a different kernel size to capture spatial hierarchies at various scales. The mathematical representation of the convolution operation, which is the fundamental building block of these layers, is expressed as

$$O_{ij} = \sum_m \sum_n I_{(i+m)(j+n)} K_{mn} \tag{20}$$

Here, O_{ij} is the output at position (i, j), I represents the input image matrix, and K is the kernel matrix. The convolution layers are designed to extract various features from the input image, with each kernel K learning to recognize a specific feature.

After passing through the Inception modules, the feature maps are processed through additional layers tailored explicitly for the regression task. These layers are chosen and structured to tune the network better. Firstly, pooling layers reduce the spatial dimensions of the feature maps, decreasing the computational complexity and enhancing the network's ability to capture the most salient features.

The final stage of the model consists of dense layers, which are fully connected layers and use a ReLu activation function. These layers integrate the learned features into predictions. To this aim, the last layer, with only two outputs, uses a linear activation function. The output of the last dense layer is the regression prediction, calculated as

$$y = \mathbf{W}^T \mathbf{x} + b \tag{21}$$

In this equation, $\mathbf{x}$ represents the input feature vector from the preceding layers, $\mathbf{W}$ is the weight matrix of the dense layer, and b is the bias term. This final layer is crucial as it maps the extracted features to the continuous output space of the regression task.

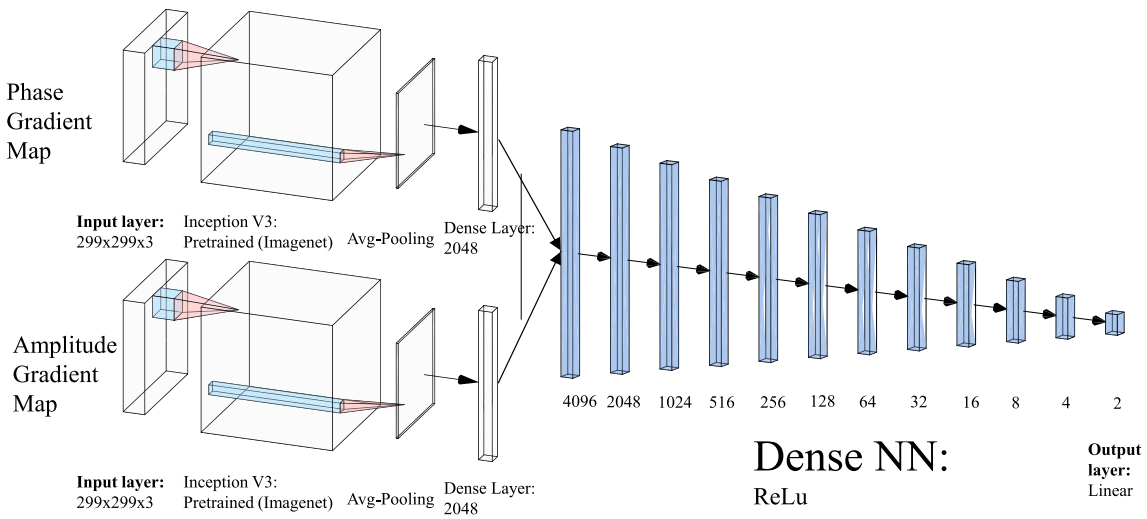

Fig. 6 The considered NN architecture to estimate the nugget and corona bond diameters from phase and amplitude gradient maps

The model's training involves optimizing a loss function using the Adam optimizer, a variant of stochastic gradient descent. The Adam optimizer adjusts the learning rate dynamically, offering advantages in convergence speed and stability. The update rule for weights in Adam is given by

$$\theta_{t+1} = \theta_t - \frac{\eta}{\sqrt{\hat{v}_t} + \epsilon}\hat{m}_t \tag{22}$$

where θ_t are the parameters at time t, η is the learning rate, $\hat{m}_t$ and $\hat{v}_t$ are estimates of the first and second moments of the gradients, and ϵ is a small scalar added for numerical stability.

Model performance evaluation is based on metrics relevant to regression analysis. We selected as loss function $\mathcal{L}$ the mean squared error (MSE) defined as

$$\mathcal{L} = \frac{1}{n}\sum_{i=1}^{n}(y_i - \hat{y}_i)^2 \tag{23}$$

where y_i are the true values, $\hat{y}_i$ are the predicted values, and n is the number of samples.

The algorithm ran on a laptop PC with an Intel Core i7-11800 H processor, 32 GB of RAM, and an Nvidia RTX 3060 GPU. The neural network has been developed using TensorFlow and Keras libraries, and the computation has been performed on the Windows Subsystem for Linux (WSL) in order to use the CUDA driver to run the training on the GPU. Regarding the hyperparameters, the loss function used is the means squared error, and the optimizer is Adam, with an initial learning rate of 0.001. A learning rate scheduler has also been used to monitor the minimum validation loss and halve the learning rate after 50 epochs of the plateau. After 150 epochs, the weights are saved every time the validation loss reaches its minimum. Figure 7 presents the training and validation loss behavior.

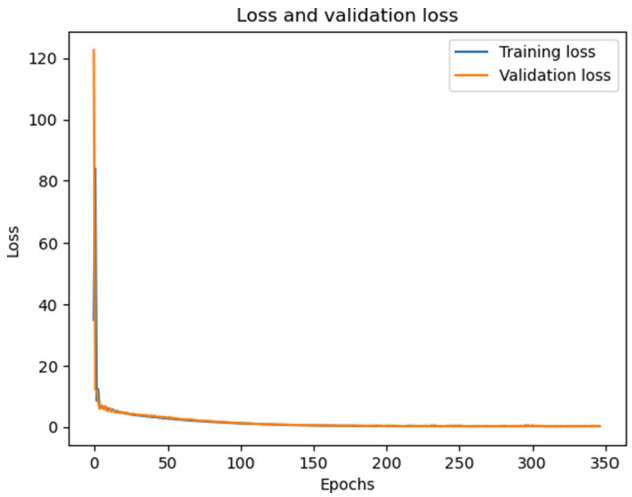

Fig. 7 Validation and training behaviors

3.5 Fine-tuning

Fine-tuning is essential to tailor the pre-trained InceptionV3 model to our specific regression task. This process involves several key stages.

Initially, we leverage the InceptionV3 model pre-trained on a large and diverse dataset, like ImageNet. This pre-training provides a robust set of learned features, representing a valuable starting point, especially when dealing with limited training data. From the given images, the pre-trained NN captures generic features that can be made more application-specific during fine-tuning.

Once we get an optimal parameter set for the dense NN layers through the pre-trained model, we selectively unfreeze some InceptionV3 layers for training. This is a critical step in fine-tuning, as it allows the model to adjust its pre-learned weights and learn more specific features from our dataset. The decision of which layers to unfreeze is based on the network depth and task complexity. Typically, layers closer to the input learn more generic features, while deeper layers learn more specific features. Thus, we often unfreeze the deeper layers while keeping the initial layers frozen, leading to

$$W_{new} = W_{old} - \alpha \cdot \frac{\partial \mathcal{L}}{\partial W}, \tag{24}$$

where W_{new} and W_{old} are the updated and previous weights, respectively, α represents the learning rate, and $\frac{\partial \mathcal{L}}{\partial W}$ is the gradient of the loss function with respect to the weights. Compared to the initial training phase, a lower learning rate is typically used during fine-tuning, ensuring that the model's pre-learned weights are not drastically altered, allowing for subtle adjustments. This fine-tuning with a lower learning rate helps the model adapt to the specific features of our dataset while retaining the general feature-detection capabilities learned during pre-training.

Finally, the model is trained on our specific dataset. This training allows the unfrozen layers to adjust their weights and learn patterns and features relevant to our regression task. This step is crucial for the model transitioning from recognizing general image features to understanding nuances specific to our dataset and regression objectives.

Through this process of fine-tuning, we effectively adapt the comprehensive feature-detection capabilities of the InceptionV3 model to our specific regression needs. The combination of pre-trained knowledge and task-specific learning results in a powerful model capable of making accurate predictions based on our dataset.

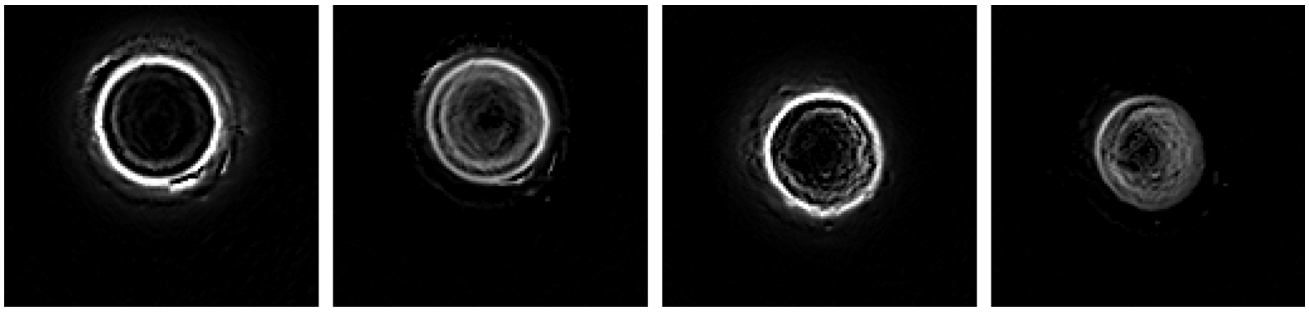

Fig. 8 Comparison of adjusted maps for different nugget sizes

As regards the algorithm, the model compile was the same, but a starting learning rate of 0.0001 was used. The Dense layers have been frozen during this phase, so not being trainable, and the first and last 50 layers of the InvecptionV3 NN have been unfrozen and made trainable.

4 Results and discussion

To distinguish between the two different diameters, nugget and corona bond, in a non-destructive manner, a neural network is employed to retrieve the data as described in Sect. 3. The methodology has an effective physical basis. Still, in the context of industry automation, it is crucial to have an automated approach for evaluating and assessing quality control measurements. Figure 8 illustrates two examples of phase maps and amplitude maps that have been adjusted and normalized. There is a distinct and discernible nugget within the observed image.

However, using a binarization thresholding algorithm to assess the diameter proves to be challenging. Hence, the neural network is utilized. The amplitude gradient shows where there is a steep change in the thermal signal amplitude. The main changes within the RSW are, for sure, where the two slabs are not joined anymore, so on the external diameter of the corona bond, and in the nugget where there is a microstructural change because the metal was molten. Martensite has an almost halved thermal diffusivity [68] to pearlite or ferrite. In the internal part of the nugget, there is a noisy signal, similarly to the C-scan from [17], showing an incredible similarity between ultrasonic and thermographic testing.

In general, the amplitude shows a larger gradient magnitude to the phase in the irregularity corresponding to the external diameter of the corona bond. It is easy to think that the thermal wave finds a larger resistance when the two sheets are no longer joined. Meanwhile, the phase image shows a better imaging quality for nugget detection. That is why both images have been chosen as inputs for the neural network, allowing the accurate estimation of both features.

The neural network can predict the diameter of the nugget and the corona bond. Figure 9 displays the estimated nugget diameter for the training and validation datasets, along with their respective linear regression lines. The achieved

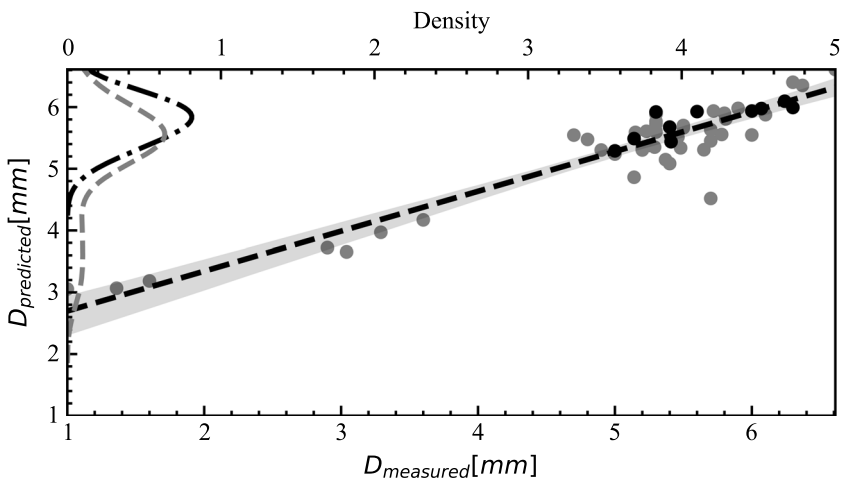

Fig. 9 Nugget estimates from NN and kernel density estimation (upper axis). In grey, the training data, and in black, the validation data

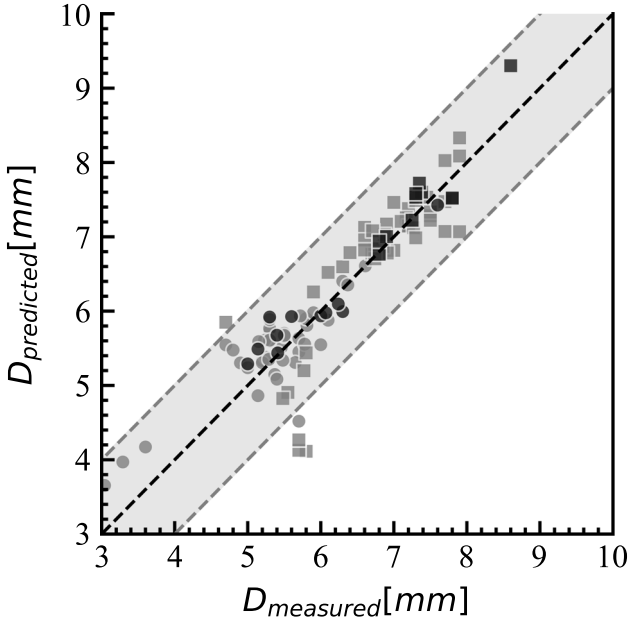

Fig. 10 Nugget (dots) and corona bond (squares) for the training dataset (gray) and the validation dataset (black)

validation loss is around one before the fine-tuning and 0.08 after it. The kernel density estimation is plotted on the left axis to demonstrate the statistical distribution of the nugget diameters in both datasets. Despite a few outliers, the algorithm appears to exhibit good accuracy. The outliers are related to the welding points positioned in the left zone of the lobe diagram, namely points where the nugget and the corona bond are not sufficiently large. These conditions are also not of industrial interest; it is much more useful to study the excessive diameters of the spot due to, for example, electrode wear.

However, it is essential to note that the measurement of the nugget and corona bond in experiments may be prone to error, as it relies on a subjective interpretation of a micrograph, and the welded part may not always exhibit a clear microstructural difference between the nugget and corona bond.

Figure 10 presents the estimate of the nugget and corona bond diameters versus their actual value. It is possible to see that almost all the points for both plots lie inside the confidence bound of ± 1 mm. The nugget diameter prediction has a Pearson coefficient $\rho = 0.938$, while the corona bond diameter prediction has a Pearson coefficient of $\rho = 0.913$.

In [66], authors demonstrate that as we move towards welded points with a larger diameter, the nugget gets significantly closer to the CB; therefore, if we exclude the points with insufficient nugget diameter and focus only on nuggets larger than four times the square root of the thickness of the sheet, we would obtain better estimates of the CB.

5 Conclusion

This study has elucidated the critical role of RSW in achieving efficient and cost-effective metal joining across various industrial applications. Through an in-depth investigation, we have highlighted the limitations of traditional destructive testing methods in assessing the quality of spot welds, underscoring the need for innovative, non-destructive evaluation techniques to ensure joint integrity and performance.

Our findings reveal that alternative assessment methodologies can significantly enhance the predictability and reliability of weld quality, thereby mitigating potential failures in structural applications. We demonstrated the potential for real-time monitoring and quality assessment of RSW processes by integrating advanced analytical tools and machine learning algorithms.

The implications of our research are several, offering a path toward more sustainable and efficient manufacturing processes. By reducing reliance on destructive testing, we not only conserve materials and reduce waste but also streamline the production pipeline, resulting in cost savings and environmental benefits.

Future research should aim to refine these non-destructive evaluation techniques, explore their applicability across different welding scenarios, and further integrate them with industrial automation systems. The development of standardized protocols for implementing these methodologies will be crucial in their adoption and effectiveness in ensuring weld quality.

In conclusion, our study contributes to the knowledge of RSW by providing insight into alternative quality assessment methods, paving the way for more resilient and sustainable industrial practices. As the demand for high-quality welding continues to grow, the innovations brought forth by this research will undoubtedly play a pivotal role in meeting the challenges of modern manufacturing processes.

Funding Open access funding provided by Politecnico di Torino within the CRUI-CARE Agreement.

Declarations

Conflict of interest The authors declare a potential Conflict of interest related to this work. The subject matter of this manuscript is covered under the patent application no. 102023000023949 filed by the Politecnico di Torino.

Open Access This article is licensed under a Creative Commons Attribution 4.0 International License, which permits use, sharing, adaptation, distribution and reproduction in any medium or format, as long as you give appropriate credit to the original author(s) and the source, provide a link to the Creative Commons licence, and indicate if changes were made. The images or other third party material in this article are included in the article's Creative Commons licence,

unless indicated otherwise in a credit line to the material. If material is not included in the article's Creative Commons licence and your intended use is not permitted by statutory regulation or exceeds the permitted use, you will need to obtain permission directly from the copyright holder. To view a copy of this licence, visit http://creativecommons.org/licenses/by/4.0/.

References

1. Rajarajan C, Sonar T, Sivaraj P, Raja S, Mathiazhagan N (2022) Investigating the effect of electrode pressure on nugget size, microstructure and tensile shear strength of resistance spot welded advanced high strength dual phase steel joints. Metallography Microstruct Anal 11(3):472–483. https://doi.org/10.1007/s13632-022-00862-x
2. Javaheri E, Lubritz J, Graf B, Rethmeier M (2020) Mechanical properties characterization of welded automotive steels. Metals 10(1):1. https://doi.org/10.3390/met10010001
3. Pouranvari M (2011) Effect of welding parameters on the peak load and energy absorption of low-carbon steel resistance spot welds. ISRN Mech Eng 2011:824149. https://doi.org/10.5402/2011/824149
4. Pouranvari M, Abedi A, Marashi P, Goodarzi M (2008) Effect of expulsion on peak load and energy absorption of low carbon steel resistance spot welds. Sci Technol Weld Join 13(1):39–43. https://doi.org/10.1179/174329307X249342
5. Panza L, Bruno G, Antal G, De Maddis M, Russo Spena P (2024) Machine learning tool for the prediction of electrode wear effect on the quality of resistance spot welds. Int J Interact Des Manuf 1–18. https://doi.org/10.1007/S12008-023-01733-7/FIGURES/15
6. Summerville C, Compston P, Doolan M (2019) A comparison of resistance spot weld quality assessment techniques. Procedia Manuf 29:305–312. https://doi.org/10.1016/j.promfg.2019.02.142. "18th International Conference on Sheet Metal, SHEMET 2019" "New Trends and Developments in Sheet Metal Processing"
7. AWS (2013) D8.1M:2013 - Specification for automotive weld quality - resistance spot welding of steel
8. AWS (2022) D8.9M:2022 - Test methods for evaluating the resistance spot welding behavior of automotive sheet steel materials
9. Hussein KM, Akbari H, Noorossana R, Yadegari R, Ashiri R (2023) Mechanical behavior investigation for quenching and partitioning steel dissimilar resistance spot welds. J Materials Res Tech 27:4064–4073. https://doi.org/10.1016/j.jmrt.2023.10.220
10. Li W (2004) Modeling and on-line estimation of electrode wear in resistance spot welding. J Manuf Sci Eng 127(4):709–717. https://doi.org/10.1115/1.2034516
11. Peng J, Fukumoto S, Brown L, Zhou N (2004) Image analysis of electrode degradation in resistance spot welding of aluminium. Science and Technology of Welding and Joining 9(4):331–336. https://doi.org/10.1179/136217104225012256
12. Zhang XQ, Chen GL, Zhang YS (2008) Characteristics of electrode wear in resistance spot welding dual-phase steels. Materials Des 29(1):279–283. https://doi.org/10.1016/j.matdes.2006.10.025
13. Dahmene F, Yaacoubi S, Mahjoub EM, Bouzenad AE, Rabaey P, Masmoudi M, Nennig P, Dupuy T, Benlatreche Y, Taram A (2022) On the nondestructive testing and monitoring of cracks in resistance spot welds: recent gained experience. Welding in the World 66:629–641. https://doi.org/10.1007/s40194-022-01249-w
14. Martín Ó, Pereda M, Santos JI, Galán JM (2014) Assessment of resistance spot welding quality based on ultrasonic testing and tree-based techniques. J Materials Process Tech 214(11):2478–2487. https://doi.org/10.1016/j.jmatprotec.2014.05.021
15. Zhou K, Yao P (2019) Overview of recent advances of process analysis and quality control in resistance spot welding. Mech Syst Signal Process 124:170–198. https://doi.org/10.1016/j.ymssp.2019.01.041
16. Misokefalou E, Papoutsidakis M, Priniotakis G (2022) Non-destructive testing for quality control in automotive industry. Int J Eng Appl Sci Tech 7(1):349–355. https://doi.org/10.33564/ijeast.2022.v07i01.054
17. Zhang B, Zhang B, Cai W, Wang L, Zhang Y (2021) A novel method to eliminate the corona bond effect in detecting resistance spot welding joints based on ultrasonic vortex C-Scan technique. Int J Adv Manufact Tech 117(11–12):3241–3252. https://doi.org/10.1007/s00170-021-07875-w
18. Cantini L, Cucchi M, Fava G, Poggi C (2012) Fourier analysis applied to infrared thermography of fiber composites used for the strengthening of structural elements. In: Proceedings of the 11th international conference on quantitative infrared thermography, pp 1–9. QIRT Council. https://doi.org/10.21611/qirt.2012.392
19. Song J, Gao B, Woo WL, Tian GY (2020) Ensemble tensor decomposition for infrared thermography cracks detection system. Infrared Phys Tech 105:103203. https://doi.org/10.1016/j.infrared.2020.103203
20. Rajic N (2002) Principal component thermography for flaw contrast enhancement and flaw depth characterisation in composite structures. Compos Struct 58(4):521–528. https://doi.org/10.1016/S0263-8223(02)00161-7
21. Huang K-L, Sfarra S, Wen C-M, Yao Y, Zhao C (2021) Exploratory factor analysis for defect identification with active thermography. Meas Sci Tech 32(11):114010. https://doi.org/10.1088/1361-6501/ac17f9
22. Maierhofer C, Röllig M, Steinfurth H, Ziegler M, Kreutzbruck M, Scheuerlein C, Heck S (2012) Non-destructive testing of Cu solder connections using active thermography. NDT E Int 52:103–111. https://doi.org/10.1016/j.ndteint.2012.07.010
23. Guo X, Vavilov V (2013) Crack detection in aluminum parts by using ultrasound-excited infrared thermography. Infrared Phys Tech 61:149–156. https://doi.org/10.1016/j.infrared.2013.08.003
24. Zhou Q, Rong Y, Shao X, Jiang P, Gao Z, Cao L (2018) Optimization of laser brazing onto galvanized steel based on ensemble of metamodels. J Intell Manufact 29(7):1417–1431. https://doi.org/10.1007/s10845-015-1187-5
25. Hagqvist P, Sikström F, Christiansson A-K, Lennartson B (2014) Emissivity compensated spectral pyrometry for varying emissivity metallic measurands. Meas Sci Tech 25(2):025010. https://doi.org/10.1088/0957-0233/25/2/025010
26. Honner M, Litoš P, Švantner M (2004) Thermography analyses of the hole-drilling residual stress measuring technique. Infrared Phys Tech 45(2):131–142. https://doi.org/10.1016/j.infrared.2003.08.001
27. Paoloni S, Tata ME, Scudieri F, Mercuri F, Marinelli M, Zammit U (2010) IR thermography characterization of residual stress in plastically deformed metallic components. Appl Phys A 98(2):461–465. https://doi.org/10.1007/s00339-009-5422-9
28. Susa M, Maldague X, Svaic S, Boras I, Bendada A (2008) The influence of surface coatings on the differences between numerical and experimental results for samples subject to a pulse thermography examination. In: Proceedings of the 9th international conference on quantitative infrared thermography, pp 1–8. QIRT Council. https://doi.org/10.21611/qirt.2008.12_11_16
29. Meng X, Wang Y, Liu J, He W (2019) Nondestructive inspection of curved clad composites with subsurface defects by combination active thermography and three-dimensional (3D) structural optical

imaging. Infrared Phys Tech 97:424–431. https://doi.org/10.1016/j.infrared.2019.01.026
30. Runnemalm A, Ahlberg J, Appelgren A, Sjökvist S (2014) Automatic inspection of spot welds by thermography. J Nondestruct Eval 33(3):398–406. https://doi.org/10.1007/s10921-014-0233-0
31. Bagavathiappan S, Lahiri BB, Saravanan T, Philip J, Jayakumar T (2013) Infrared thermography for condition monitoring - a review. Infrared Phys Technol 60:35–55. https://doi.org/10.1016/j.infrared.2013.03.006
32. Pitarresi G, Cappello R, Capraro A, Pinto V, Badagliacco D, Valenza A (2023) Frequency modulated thermography-NDT of polymer composites by means of human-controlled heat modulation. In: Rizzo P, Milazzo A (eds) European workshop on structural health monitoring, pp 610–618. Springer. https://doi.org/10.1007/978-3-031-07258-1_62
33. Sirikham A, Zhao Y, Liu H, Xu Y, Williams S, Mehnen J (2020) Three-dimensional subsurface defect shape reconstruction and visualisation by pulsed thermography. Infrared Phys Technol 104:103151. https://doi.org/10.1016/j.infrared.2019.103151
34. Sadiq H, Wong MB, Tashan J, Al-Mahaidi R, Zhao X-L (2013) Determination of steel emissivity for the temperature prediction of structural steel members in fire. J Mater Civ Eng 25(2):167–173. https://doi.org/10.1061/(ASCE)MT.1943-5533.0000607
35. Bang H-T, Park S, Jeon H (2020) Defect identification in composite materials via thermography and deep learning techniques. Compos Struct 246:112405. https://doi.org/10.1016/j.compstruct.2020.112405
36. Maierhofer C, Myrach P, Krankenhagen R, Röllig M, Steinfurth H (2015) Detection and characterization of defects in isotropic and anisotropic structures using lockin thermography. J Imaging 1(1):220–248. https://doi.org/10.3390/jimaging1010220
37. Da Silva WF, Melo RAC, Grosso M, Pereira GR, Riffel DB (2020) Active thermography data-processing algorithm for nondestructive testing of materials. IEEE Access 8:175054–175062. https://doi.org/10.1109/ACCESS.2020.3025329
38. Rajic N, Antolis C (2017) An investigation of noise performance in optical lock-in thermography. Infrared Phys Technol 87:1–10. https://doi.org/10.1016/j.infrared.2017.09.019
39. Grys S, Vokorokos L, Borowik L (2014) Size determination of subsurface defect by active thermography – simulation research. Infrared Phys Technol 62:147–153. https://doi.org/10.1016/j.infrared.2013.11.011
40. Srajbr C (2016) Induction excited thermography in industrial applications. In: Proceedings of 19th world conference on nondestructive testing (WCNDT 2016), vol 21, pp 1–9
41. Jonietz F, Myrach P, Suwala H, Ziegler M (2015) Examination of spot welded joints with active thermography. J Nondestruct Eval 35(1):1. https://doi.org/10.1007/s10921-015-0318-4
42. Sesana R, Santoro L, Curà F, Molica Nardo R, Pagano P (2023) Assessing thermal properties of multipass weld beads using active thermography: microstructural variations and anisotropy analysis. International Journal of Advanced Manufacturing Technology. https://doi.org/10.1007/s00170-023-11951-8
43. Santoro L, Sesana R, Molica Nardo R, Curá F (2023) Infrared in-line monitoring of flaws in steel welded joints: a preliminary approach with SMAW and GMAW processes. International Journal of Advanced Manufacturing Technology. https://doi.org/10.1007/s00170-023-12044-2
44. Huang J, Pastor ML, Garnier C, Gong XJ (2019) A new model for fatigue life prediction based on infrared thermography and degradation process for CFRP composite laminates. Int J Fatigue 120:87–95. https://doi.org/10.1016/j.ijfatigue.2018.11.002
45. Park H, Choi M, Park J, Kim W (2014) A study on detection of micro-cracks in the dissimilar metal weld through ultrasound infrared thermography. Infrared Phys Technol 62:124–131. https://doi.org/10.1016/j.infrared.2013.10.006
46. Cheng Y, Bai L, Yang F, Chen Y, Jiang S, Yin C (2016) Stainless steel weld defect detection using pulsed inductive thermography. IEEE Trans Appl Supercond 26(7):1–4. https://doi.org/10.1109/TASC.2016.2582662
47. Yuan B, Spiessberger C, Waag TI (2017) Eddy current thermography imaging for condition-based maintenance of overlay welded components under multi-degradation. Marine Struct 53:136–147. https://doi.org/10.1016/j.marstruc.2017.02.001
48. García de la Yedra A, Fernández E, Beizama A, Fuente R, Echeverria A, Broberg P, Runnemalm A, Henrikson P (2014) Defect detection strategies in nickel superalloys welds using active thermography. In: Proceedings of the 12th international conference on quantitative infrared thermography, pp 1–8. QIRT Council. https://doi.org/10.21611/qirt.2014.028
49. Broberg P (2013) Surface crack detection in welds using thermography. NDT E Int 57:69–73. https://doi.org/10.1016/j.ndteint.2013.03.008
50. Li T, Almond DP, Rees DAS (2011) Crack imaging by scanning pulsed laser spot thermography. NDT E Int 44(2):216–225. https://doi.org/10.1016/j.ndteint.2010.08.006
51. Schlichting J, Brauser S, Pepke L-A, Maierhofer C, Rethmeier M, Kreutzbruck M (2012) Thermographic testing of spot welds. NDT E Int 48:23–29. https://doi.org/10.1016/j.ndteint.2012.02.003
52. D'Accardi E, De Finis R, Dell'Avvocato G, Masciopinto G, Palumbo D, Galietti U (2024) Conduction thermography for non-destructive assessment of fatigue cracks in metallic materials. Infrared Phys Technol 140:105394. https://doi.org/10.1016/J.INFRARED.2024.105394
53. Dell'Avvocato G, Gohlke D, Palumbo D, Krankenhagen R, Galietti U (2022) Quantitative evaluation of the welded area in Resistance Projection Welded (RPW) thin joints by pulsed laser thermography. In: Mendioroz A, Avdelidis NP (eds) Thermosense: Thermal Infrared Applications XLIV, vol 12109, p 121090. SPIE. https://doi.org/10.1117/12.2618806. International Society for Optics and Photonics
54. Dell'Avvocato G, Palumbo D, Palmieri ME, Galietti U (2022) Non-destructive thermographic method for the assessment of heat treatment in boron steel. In: Mendioroz A, Avdelidis N.P (eds) Thermosense: Thermal infrared applications XLIV, vol 12109, p 1210906. SPIE. https://doi.org/10.1117/12.2618810 . International Society for Optics and Photonics
55. Dell'Avvocato G, Rashkovets M, Castellano A, Palumbo D, Contuzzi N, Casalino G, Galietti U (2024) Preliminary procedure for the assessment of probeless friction stir spot welds (P-FSSW) in dissimilar aluminum alloys by long pulsed laser thermography, 17. https://doi.org/10.1117/12.3013618
56. Strzałkowski K, Streza M, Dadarlat D, Marasek A (2015) Thermal characterization of II-VI binary crystals by photopyroelectric calorimetry and infrared lock-in thermography. J Therm Anal Calorim 119(1):319–327. https://doi.org/10.1007/s10973-014-4137-0
57. Mendioroz A, Fuente-Dacal R, Apiñaniz E, Salazar A (2009) Thermal diffusivity measurements of thin plates and filaments using lock-in thermography. Rev Sci Instrum 80(7):074904. https://doi.org/10.1063/1.3176467
58. Philipp A, Pech-May NW, Kopera BAF, Lechner AM, Rosenfeldt S, Retsch M (2019) Direct measurement of the in-plane thermal diffusivity of semitransparent thin films by lock-in thermography: an extension of the slopes method. Anal Chem 91(13):8476–8483. https://doi.org/10.1021/acs.analchem.9b01583
59. Santoro L, Razza V, De Maddis M (2023) Frequency-based analysis of active laser thermography for spot weld quality assessment. Int J Adv Manuf Technol. https://doi.org/10.1007/s00170-023-12845-5
60. Zhang Z, Li B, Zhang W, Lu R, Wada S, Zhang Y (2020) Real-time penetration state monitoring using convolutional neural network

for laser welding of tailor rolled blanks. J Manuf Syst 54:348–360. https://doi.org/10.1016/J.JMSY.2020.01.006
61. Cifuentes Á, Mendioroz A, Salazar A (2017) Simultaneous measurements of the thermal diffusivity and conductivity of thermal insulators using lock-in infrared thermography. Int J Thermal Sci 121:305–312. https://doi.org/10.1016/j.ijthermalsci.2017.07.023
62. Kato H, Baba T, Okaji M (2001) Anisotropic thermal-diffusivity measurements by a new laser-spot-heating technique. Meas Sci Technol 12(12):2074. https://doi.org/10.1088/0957-0233/12/12/307
63. Allen RL, Mills DW (2004) Signal Analysis: Time, Frequency, Scale, and Structure. John Wiley & Sons. https://doi.org/10.1002/047166037X
64. AWS (2019) C1.1M/C1.1:2019 - Recommended practices for resistance welding
65. ISO Central Secretary (2021) Resistance welding - Vocabulary - Part 1: spot, projection and seam welding. Standard BS EN ISO 17677-1:2021, International Organization for Standardization, Geneva, CH
66. Ma Y, Takikawa A, Nakanishi J, Doira K, Shimizu T, Lu Y, Ma N (2021) Measurement of local material properties and failure analysis of resistance spot welds of advanced high-strength steel sheets. Mater Des 201:109505. https://doi.org/10.1016/j.matdes.2021.109505
67. Liu S, Deng W (2015) Very deep convolutional neural network based image classification using small training sample size. In: 2015 3rd IAPR Asian conference on pattern recognition (ACPR), pp 730–734. https://doi.org/10.1109/ACPR.2015.7486599
68. Dell'Avvocato G, Palumbo D, Galietti U (2023) A non-destructive thermographic procedure for the evaluation of heat treatment in Usibor®1500 through the thermal diffusivity measurement. NDT E Int 133. https://doi.org/10.1016/j.ndteint.2022.102748

Publisher's Note Springer Nature remains neutral with regard to jurisdictional claims in published maps and institutional affiliations.